

Average energy of the X-ray spectrum as a model-independent proxy for the mass of galaxy clusters

Aleksei Kruglov¹*, Ildar Khabibullin^{2,3,1}, Natalya Lyskova¹, Klaus Dolag^{2,3}, and Veronica Biffi^{4,5}

¹Space Research Institute (IKI), Profsoyuznaya 84/32, Moscow 117997, Russia

²Universitäts-Sternwarte, Fakultät für Physik, Ludwig-Maximilians-Universität München, Scheinerstr. 1, D-81679 München, Germany

³Max Planck Institute for Astrophysics, Karl-Schwarzschild-Str. 1, D-85741 Garching, Germany

⁴INAF, Osservatorio Astronomico di Trieste, via Tiepolo 11, I-34131, Trieste, Italy

⁵IFPU – Institute for Fundamental Physics of the Universe, Via Beirut 2, I-34014 Trieste, Italy

Accepted XXX. Received YYY; in original form ZZZ

ABSTRACT

Temperature of the hot gas in galaxy clusters is known to be a reliable proxy for their total gravitating mass, allowing one to use spectroscopic X-ray observations for halo mass function measurements. Data of shallow wide area surveys, however, often precludes direct fitting of the X-ray spectra, given possible biases arising due to unresolved (multitemperature) inner structure of the intracluster medium (ICM), projection effects and necessity of certain model assumptions to be made to allow for robust spectral fitting. We consider using a simple observable value - the average energy of the observed cluster X-ray spectrum - as a model-independent proxy for the ICM temperature, and consequently cluster's mass. We calibrate relation of this proxy to the cluster parameters using mock observations for a sample of 84 massive galaxy clusters extracted from the *Magneticum* cosmological hydro simulations. We consider observational parameters corresponding to the all-sky survey observations by *SRG/eROSITA*. Taking into account contributions of various background and foreground signals, average energy of the simulated X-ray spectra in the 0.4 – 7.0 keV band is shown to be a stable indicator of the ICM temperature with $\sim 10\%$ scatter and cluster's mass M_{500} with a $\sim 20\%$ scatter. A database containing simulated X-ray images and their spectra (subtracted in several concentric rings) is publicly available.

Key words: X-rays: galaxies: clusters – galaxies: clusters: intracluster medium

1 INTRODUCTION

Number density of massive (with virial mass $\gtrsim 10^{14}M_{\odot}$) galaxy clusters and their spatial distribution reflect cosmological evolution of the Universe, governed in particular by its dark matter and dark energy content, as well as power spectrum of the initial density perturbations. Thanks to that, measurements of the halo mass function (i.e. number density as a function of mass) for galaxy clusters have been successively used to infer values of corresponding parameters of the Λ Cold Dark Matter (Λ CDM) cosmological model, in particular relative matter Ω_M and dark energy Ω_{Λ} density, amplitude of linear density fluctuations σ_8 and the spectral index n of primordial fluctuations (Kravtsov & Borgani 2012, for a recent review).

Masses of galaxy clusters¹ can be determined directly only through

gravitational lensing measurements, which, however, are accompanied by systematic effects such as presence of large-scale structures along the line-of-sight, assumed underlying dark matter distribution, and shear from massive substructures (e.g. Meneghetti et al. 2010; Hoekstra 2003). On the other hand, the cluster mass can be determined implicitly from properties of its intracluster medium (ICM) which can be inferred from observations of its thermal X-ray emission (e.g. Sarazin 1986; Böhringer & Werner 2010) or Sunyaev-Zeldovich distortion of the Cosmic Microwave Background radiation (Sunyaev & Zeldovich 1972) in their direction.

Several quantities derivable from X-ray and microwave observations were put forward as proxies for cluster mass estimation, among them total X-ray luminosity (Kaiser 1986), spectral temperature of the thermal X-ray emission (Markevitch 1998; Arnaud & Evrard 1999; Vikhlinin et al. 2006), mass estimate of the X-ray emitting gas (Vikhlinin et al. 2003), or the so-called Y_X parameter (the product of the ICM mass and its temperature, Kravtsov et al. 2006). Accurate measurements of these quantities for large samples of galaxy clusters is, however, challenging, especially in the regime of low mass clusters and shallow observations delivered by modern wide area surveys.

Moreover, given the multitemperature inner structure of the ICM, its average temperature could be defined in several ways. For instance, one can use data of cosmological hydrodynamical simulations that carry information about density, temperature and vol-

* E-mail: kruglov@cosmos.ru

¹ As a galaxy cluster halo doesn't have a distinct boundary, the definition of cluster mass needs to be clarified. To avoid ambiguity, throughout this paper this quantity will be considered as M_{500} , i.e. mass enclosed inside the sphere of radii R_{500} (within which the mean density is equal to 500 times the critical density of the Universe at the epoch of observation). This choice of overdensity is a compromise between theoretical requirements (driven by numerical resolution in simulations, accounting for non-gravitational effects, hydrostatic equilibrium assumptions etc.) and observational uncertainties, which inevitably arise for smaller values of overdensity.

umetric density of every ICM mass element to derive volume or mass-averaged temperature of the hot gas. Given that luminosity of the thermal X-ray emission scales with the square of gas density, one can also consider emission measure-weighted temperature. Observationally, the X-ray temperature is inferred via fitting the spectrum of X-ray emission with single or multi-temperature collisional ionization equilibrium (CIE) plasma emission models (e.g. APEC, Foster et al. 2012) with free or fixed abundance of the heavy elements. In many cases, however, statistical errors in the observed spectrum are too large to detect the presence of multiple emission components. Additional bias may be introduced by projection effects, i.e. accounting for photons from structures along the line-of-sight (ZuHone et al. 2023). X-ray telescope optics, namely energy-dependent effective area, is another source of temperature uncertainties (Schellenberger et al. 2015). It has been shown that the temperature derived from X-ray observations tends to be different from any of defined temperatures derived from simulations, usually underestimating them (Mathiesen & Evrard 2001; Mazzotta et al. 2004).

Compared to the cluster temperature, the X-ray luminosity (bolometric or in a certain energy range, for example, 0.5 – 2.0 keV) is a more straightforward mass proxy. However, for at fixed cluster mass, this quantity demonstrates the relatively large ($\sim 40\%$) scatter since it is very sensitive to the exact properties of the gas near the cluster core. With sufficient angular resolution, it is possible to exclude emission from cluster nuclei, thereby reducing the scatter (e.g. Markevitch 1998; Pratt et al. 2009; Bulbul et al. 2019; Eckert et al. 2020). Similar to temperature, luminosity derived from simulations and from observations may differ by a few percents and this discrepancy inevitably follows the choice of observed region; additionally, the fitting procedure required for luminosity calculations will not capture the full expected luminosity, as it requires sufficient statistics to constrain the metallicity parameter (ZuHone et al. 2023).

In this work, we propose to use an average energy of the X-ray spectrum (i.e., the value obtained by averaging nominal energies of each detector channel with weights equal to the observed count rate; see Sec. 3.3) of galaxy clusters as a temperature and mass proxy. The major advantage of presented approach is that it doesn't require any spectral fitting and is less prone to possible biases due to the multiphase structure of the gas, assumptions about cluster metallicity, and impact of masking of certain bright and relatively cool regions of ICM. In other words, the average energy works reasonably well as a mass/temperature proxy even in a case of low count statistics (at the level of few hundred total counts which are enough to identify X-ray source as an extended one but not enough for the robust spectral analysis) and provides a scatter which is comparable to mass measurements derived from temperature or luminosity. We take advantage of mock observations for a sample of galaxy clusters from the *Magneticum*² suite of state-of-the-art cosmological hydrodynamical simulations modeled for the parameters of the all-sky survey by *eROSITA* telescope (Predehl et al. 2021) of the *Spectrum-RG* observatory (Sunyaev et al. 2021). Via analysis of the predicted X-ray spectra, we calibrate the relationship between the average energy of galaxy cluster spectra and cluster temperatures and masses, and compare statistical properties of this relation to other commonly used proxies.

The paper is structured as follows: in Section 2 we briefly describe the sample of clusters used for our study and compare $T_{500} - M_{500}$ and $L_{x500} - M_{500}$ relations (where T_{500} is mass-weighted temperature and L_{x500} is bolometric X-ray luminosity, both inside the sphere of R_{500})

for them with the scaling relations derived for observed clusters. In Section 3, we perform modeling of realistic X-ray spectra, fit a single-temperature model and derive a relation between the average energy of observed cluster spectra and the cluster temperature. In Section 4, we compare luminosity, temperature and average energy as mass proxies. Finally, in Section 5, we summarize our conclusions.

2 CLUSTER SAMPLE

2.1 *Magneticum* Simulations

For our study we have used numerical cosmological hydrodynamic high-resolution simulations *Magneticum* (Hirschmann et al. 2014; Dolag et al. 2016). These simulations were performed with the TreePM/SPH code GADGET-3 (Springel 2005; Beck et al. 2016; Groth et al. 2023). They take into account many complex non-gravitational physical processes (cooling, merging of galaxies and galaxy clusters, shock waves, and detailed galaxy formation physics) which determine the evolution of large-scale systems and affect their observational properties. More details about the physics provided in the simulation can be found in Section 2 of Biffi et al. (2022) and in references therein.

For this study we have chosen *Box2/hr* simulation box. Its comoving volume is equal to $(352\text{Mpc}/h)^3$ ($h = H_0/(100 \text{ km s}^{-1} \text{ Mpc}^{-1})$ is the Hubble constant), containing $2 \cdot 1584^3$ mass resolution elements (particles). The masses of dark matter and gas particles are equal to $m_{\text{DM}} = 6.9 \cdot 10^8 M_{\odot}/h$ and $m_{\text{gas}} = 1.4 \cdot 10^8 M_{\odot}/h$, respectively, and the following cosmological parameters are adopted: the total matter density $\Omega_0 = 0.272$ (16.8% baryons), the cosmological constant $\Omega_{\Lambda} = 0.728$, the Hubble constant $H_0 = 70.4 \text{ km/s/Mpc}$ (i.e. $h = 0.704$), the index of the primordial power spectrum $n = 0.963$, the overall normalisation of the power spectrum $\sigma_8 = 0.809$ (Komatsu et al. 2011).

By means of the PHOX software package (Biffi et al. 2012, 2013; Vladutescu-Zopp et al. 2023), a 30×30 degrees lightcone was constructed based on the *Magneticum Box2/hr* simulation. To produce such mock X-ray data, first *unit1* of PHOX was used to create photons emitted by the gas mass elements (including ICM), assuming optically thin thermal emission and taking in account line emission of the various individual metal species tracked within the simulation according to the metal production yields. We neglect the predicted X-ray emission from the AGN component (Biffi et al. 2018) within the simulation although in principle available, as well as contribution of the X-ray binaries in cluster's galaxies (Vladutescu-Zopp et al. 2023). Then *unit2* of PHOX was used to create the photon list for a lightcone-like geometry, where simulation outputs at the following redshifts $z = 0.033, 0.066, 0.101, 0.137, 0.174$ where used to compose individual slices. The corresponding redshift within each slice is properly computed from the offset with respect to the center of the slice, and the photon energies are corrected for the redshift and the peculiar velocity of every resolution element within the lightcone. In addition, the corresponding meta data for the galaxy clusters within the lightcone have been created, including the redshift z_{true} (e.g. the purely cosmological) and z_{observed} (e.g. including the peculiar velocity of the cluster). The data is publicly available and can be downloaded from the data section of the *Magneticum* project webpage. Based on these halo catalogues provided for each slice of the lightcone, we have selected 84 massive clusters with $M_{500} > 10^{14} M_{\odot}/h$ as shown in Figure 1.

Several recent studies have taken advantage of a similar dataset from the *Magneticum* simulations to draw predictions regarding X-ray emission from galaxy clusters and groups. In particular, ZuHone

² <http://www.magneticum.org>

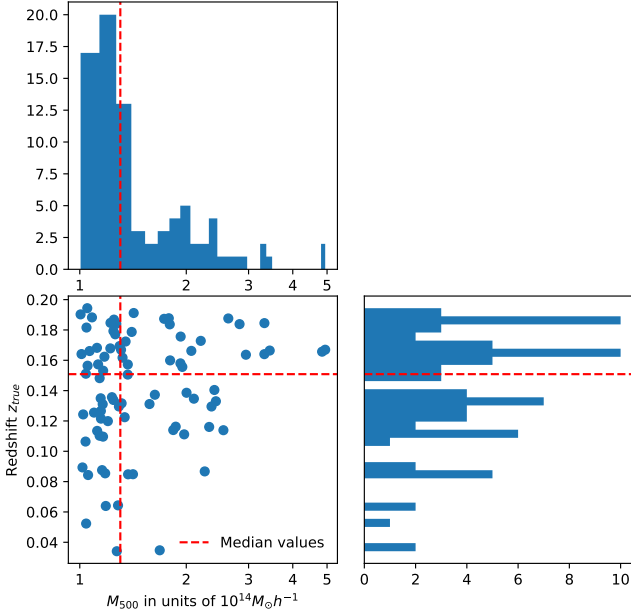


Figure 1. Histograms of masses M_{500} and redshifts z_{true} (see text for clarification) for 84 clusters in the sample. Red dashed line shows median values: $M_{500}^{\text{med}} = 1.30 \cdot 10^{14} M_{\odot}/h$ and $z_{\text{true}}^{\text{med}} = 0.15$.

et al. (2023) investigated the bias in temperature and luminosity estimates arising due to single-temperature spectral approximation and projection effects, having shown that they might be indeed significant. Angelinelli et al. (2022) have studied the properties of baryons in halos with $M_{\text{vir}} > 10^{13} M_{\odot}/h$ far beyond the virialised regions and have shown that, despite different ways of convergence which depend on their masses, these haloes have common baryon, gas, stellar and metal distributions as they approach the mean location of the accretion shock. Marini et al. (2024) have confirmed high completeness and purity of massive galaxy clusters ($M_{500} > 10^{14} M_{\odot}$) detection with *SRG/eROSITA*. Scheck et al. (2023) have investigated hydrostatic equilibrium in clusters of galaxies and have recovered temperature profiles with an accuracy on the order of 1%, providing predictions for the hydrostatic mass bias. Seppi et al. (2023) have concluded that there is good agreement in the offsets between X-ray and optical centers in clusters of galaxies measured in *eROSITA* data and the predictions from the Magneticum simulations.

Basic properties of the simulated clusters, which are relevant to our study, such as their positions inside the simulation box, redshifts z_{true} , radii R_{500} , masses M_{500} , mass-weighted temperatures T_{500} and bolometric X-ray luminosities L_{x500} are summarized in a catalogue which is made publicly available and to which we will refer to throughout this paper.

2.2 Scaling relations

As one of the key goals of the current study is to obtain relations between observable spectral properties of the X-ray emission and such parameters of the clusters as ICM temperature and total mass, we first consider the intrinsic correlations between these quantities and their consistency with the currently available observations.

In order to do so, we show how cluster parameters from the cluster catalogue, namely T_{500} and L_{x500} , correlate with the cluster mass M_{500} . We adopt the scaling relations for these quantities from Vikhlinin et al. (2009) derived for high-quality *Chandra* observations

of clusters with $0.02 < z < 0.9$ and $M_{500} \gtrsim (1-2) \times 10^{14} h^{-1} M_{\odot}$ in the form presented in Churazov et al. (2015). In these expressions, $h = H_0/100 \text{ km/s/Mpc} \equiv 0.704$ and $E(z) = \sqrt{\Omega_m(1+z)^3 + \Omega_{\Lambda}}$ where $\Omega_m = 0.272$, $\Omega_{\Lambda} = 0.728$ and z is the cluster redshift z_{true} .

According to Vikhlinin et al. (2009), the scaling between mass M_{500} and temperature is given by the following expression

$$T_X = 5 \text{ keV} \left(\frac{M_{500}}{M_0} \right)^{0.65} E(z)^{0.65} \quad (1)$$

where $M_0 = (2.95 \pm 0.10) 10^{14} h^{-1} M_{\odot}$, T_X is the gas temperature derived from a single temperature fit to the total cluster spectrum integrated within $(0.15 - 1) \cdot R_{500}$ radial range. The scatter of T_X -based mass estimations for this relation was adopted equal to 20% based on simulations from Kravtsov et al. (2006).

For the X-ray luminosity, the scaling relation from Vikhlinin et al. (2009) reads as

$$L_{X,0.5-2} = 1.2 \cdot 10^{44} \text{ erg s}^{-1} \times \left(\frac{h}{0.72} \right)^{-0.39} \left(\frac{M_{500}}{3.9 \cdot 10^{14} M_{\odot}} \right)^{1.61} E(z)^{1.85} \quad (2)$$

where $L_{X,0.5-2}$ is the rest frame cluster luminosity in the 0.5–2 keV band. For a fixed mass, the scatter in L_X reaches $\approx 48\%$.

In Fig. 2, one can see that properties of our sample of simulated clusters agree very well with the observed scaling relations. However, it is necessary to recall that T_{500} from the catalogue is a mass-weighted temperature within R_{500} , while the observationally-derived T_X is a single temperature fit to the total cluster spectrum. Therefore we don't expect perfect agreement between the simulated and observed scalings. Mathiesen & Evrard (2001) pointed out that T_X can be lower than the T_{500} by 10–20%, what indeed we observe in Fig. 2 (left panel). Also, L_{500} is the bolometric X-ray luminosity within R_{500} and therefore it doesn't strictly correspond to $L_{X,0.5-2}$. To compare the latter quantity with L_{500} we have done simple rescaling by calculating $L_{X,0.5-2}$ as a fraction of full luminosity for simulated spectra of APEC model (Foster et al. 2012) for cluster with given temperature T_X and redshift z_{true} from the catalogue. The right panel of Fig. 2 shows acceptable compliance of $L_{x500} - M$ relation for our sample of clusters, although there are some significant outliers.

3 X-RAY SPECTRAL ANALYSIS

3.1 Generating clusters images and spectra

For each cluster we generate its image with resolution equal to 4 arcseconds/pixel. We take the position of centroid of image (which is calculated by weighing the values of surface brightness in each pixel) as a reference point. This is done instead of pointing at gravitational potential minimum from the catalogue of clusters, which corresponds to the position of the main subhalo identified by the SubFind algorithm (Springel et al. 2001; Dolag et al. 2009). Despite the fact that R_{500} (but also M_{500} and T_{500}) from the simulations refer to the overdensity computed considering that the center of the cluster is located in the minimum of the potential well, the possible bias is expected to be small (Seppi et al. 2023).

We collect all photons within a cylinder with radius equal to R_{500} from the catalogue divided by angular diameter distance to the cluster obtained with redshift z_{true} from catalogue as well. The photons are gathered only from the same slice of the lightcone to which

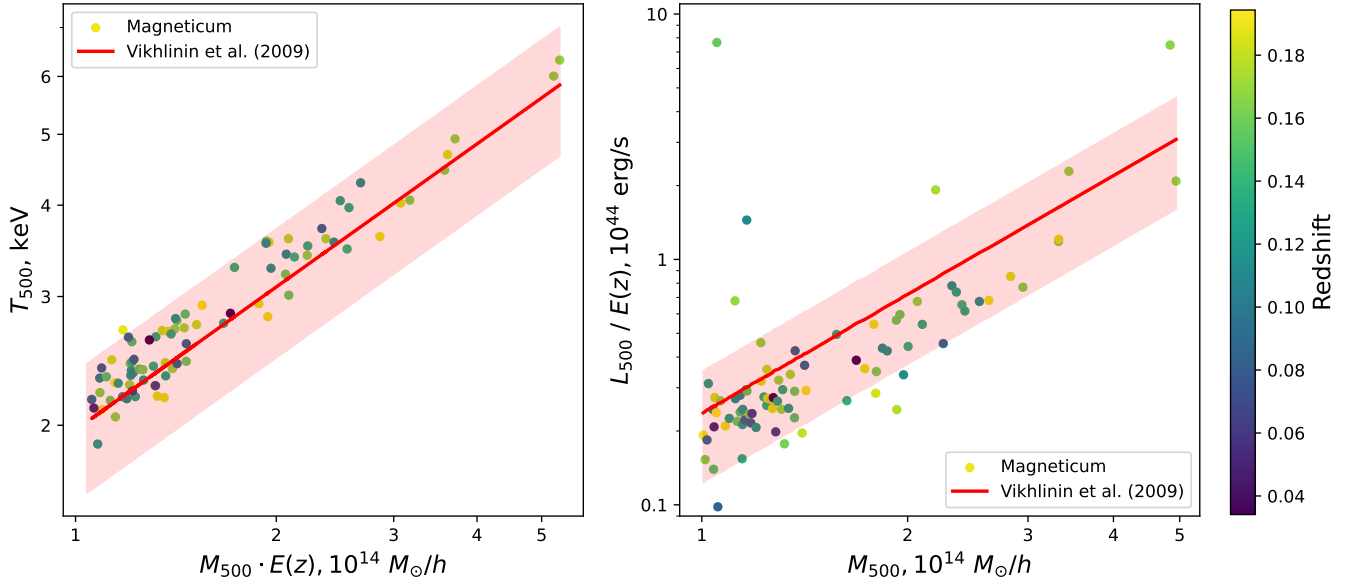


Figure 2. Scaling relations for 84 clusters from our sample. Points indicate the clusters from the *Magneticum* catalogue. Red lines show expressions (1) and (2), shaded areas show scatter from (Vikhlinin et al. 2009). Redshifts of clusters are indicated by colorbar.

the cluster belongs (i.e. the photons from other slices are not taken into account). The line-of-sight thickness of the slices, $\delta z \approx 0.033$, however, corresponds to $\gtrsim 100$ Mpc, ensuring that the correlated large-scale structures surrounding these massive clusters is included in the extracted photon lists because of the projection effect as well. For simplicity, we consider the whole sample of model clusters, although it includes objects at different dynamical and merger states. The cluster images may contain some structures that obviously stand out of the bulk ICM, for example, gas-rich galaxies. Excess of soft X-ray emission from these small "clumps" of cooler gas could have a viable contribution in the total spectrum of cluster and, therefore, can strongly shift the results of spectral analysis, leading to temperature underestimation (Mazzotta et al. 2004).

To mitigate possible undesirable effects, we do not take into account the areas that contain 5% of the brightest pixels. The loss of total photon count rate due to this filtering is 25% on average, although for some images it may reach $\sim 40\%$. However, this procedure leads to extraction of minimally contaminated spectrum, which, as will be shown below, is quite well described by the single-temperature approximation (a similar filtering was considered and quantified in Zhuravleva et al. 2013, based on the cosmological simulations). The examples of original and filtered clusters images are shown in Appendix A.

The energies of the photons collected from the circle of R_{500} centered at centroid of the X-ray image are multiplied by $(1 + z_{\text{true}})$, i.e. we consider that all clusters are observed at $z = 0$ to mitigate possible effects of redshift onto future analysis. Given that for the photons produced using PHOX the nominal observation time is 10 ks and the nominal (flat) area of instrument is 1000 cm^2 , we can treat this photon list as a X-ray flux density spectra for each cluster which then can be passed as an input model spectra to the XSPEC software (Arnaud 1996). We present³ Radially-Resolved Clusters' Spectra database (RRCS_DB) implemented as single XSPEC table model, which includes model spectra for all studied clusters along

with their images (both original and filtered). The description of this database is given in Appendix A.

3.2 Mock observations and fitting overview

We simulate galaxy cluster observations by *SRG/eROSITA* telescope, considering them to be performed by telescope module TM1 only, but with significantly long exposure equal to 10 ks. This approximately corresponds to the effective exposure per telescope module of *SRG/eROSITA* during four consecutive all-sky surveys (Lyskova et al. 2023; Merloni et al. 2024).

For each cluster, its synthetically-generated model spectrum in $0.1 - 12 \text{ keV}$ band is convolved with the *SRG/eROSITA* TM1 RMF (*Redistribution Matrix File*) and ARF (*Auxiliary Response File*) with addition of statistical fluctuations described by Poisson errors using `fakeit` command provided by XSPEC software. The resulting count spectrum is limited to the $0.4 - 7.0 \text{ keV}$ range: the upper border is motivated by the presence of the bright line at 6.7 keV (helium-like iron Fe XXV) and the lower border is limited by the prevalence of cosmic X-ray background (which will be added to the cluster spectra later) at smaller energies. The mock observation spectra are approximated by the single-temperature `phabs*apec` model with the hydrogen column density of $N_H = 10^{20} \text{ cm}^{-2}$ (since initial photons were simulated with this value of absorption) and the fixed abundance $Z = 0.3 \cdot Z_{\odot}$ (this choice is motivated by the results of numerical simulations (e.g. Biffi et al. 2017); also, our tests have shown that fixing it does not lead to any significant bias in result). We set $z = 0$ for each cluster during fitting procedure because the energies of photons have already been redshifted; temperature and normalization parameters are left free. C-statistics is applied and the weights are taken as standard. The examples of X-ray clusters spectra along with the best-fit model (with and without adding an X-ray background, which is described below) are shown in Appendix A. We denote the temperature from the best-fit model as T_{spec} .

This process is repeated 50 times for each cluster and we further consider T_{spec} as the mean value of the spectral temperature distribution. One uncorrected standard deviation is taken as the un-

³ https://github.com/pi4imu/RRCS_DB

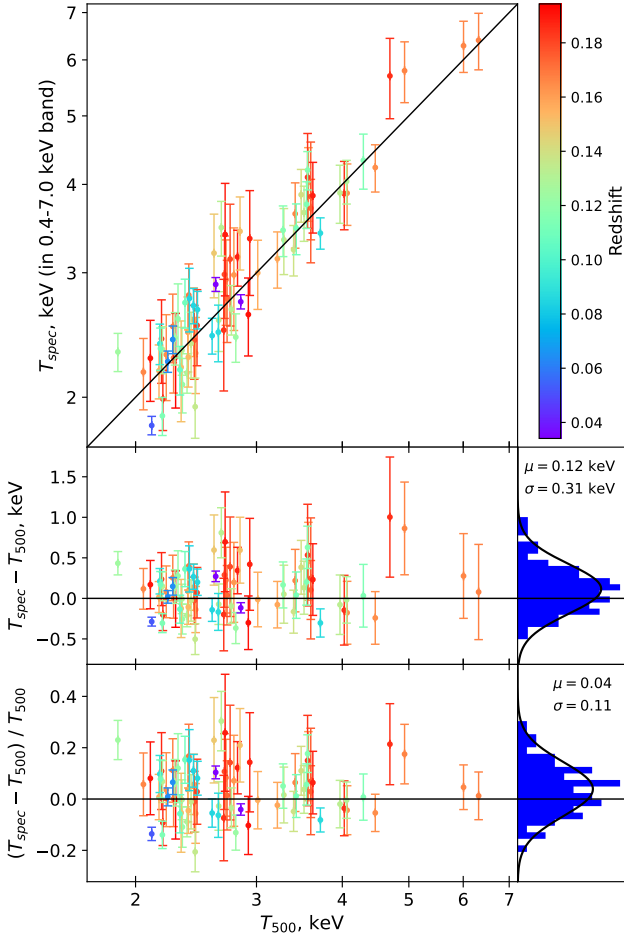


Figure 3. Comparison of the mass-weighted temperature T_{500} from the simulations with T_{spec} from spectral fitting for 84 clusters from *Magneticum* simulations. The upper panel compares temperatures directly, whereas central panel compares absolute difference and lower panel compares relative difference between them. The histograms on the right indicate mean values μ and scatter σ for this comparisons. Redshifts are indicated by colorbar. Note the log-scale for the horizontal axis.

certainty, albeit these distributions are not necessary Gaussian even in case of sufficiently many realizations, which is demonstrated in Appendix B. Figure 3 shows a comparison between T_{spec} from the single-temperature approximation and the mass-weighted T_{500} temperature taken from the catalogue for our sample of clusters. These two values are in a good agreement, which can be explained by previously described filtering of images: relatively small bright sources that could be the cause of multi-temperature structure of cluster were partially or fully excised. Also, there is no significant trend that links cluster’s redshift and its temperature, whereas errors on temperature grow almost linearly with redshift.

Simultaneously with spectral fitting, for each cluster and for each realisation we calculate the X-ray luminosity in the 0.5–2.0 keV band. Again, the mean value of its distribution is denoted as L_{spec} and one standard deviation is considered as an uncertainty. The results of this performance are described in Section 4. From mock observed spectra we also derive the value of average energy, which is described in the next section.

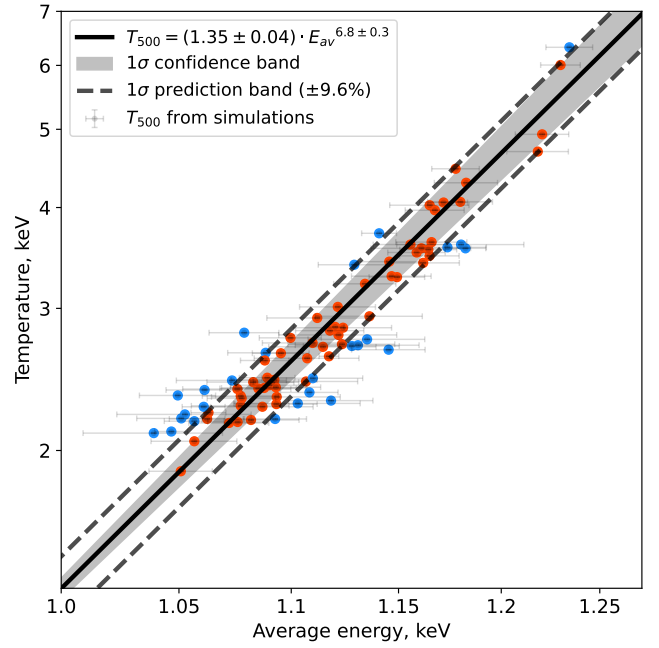


Figure 4. Temperature T_{500} as a function of the average energy E_{av} in the 0.4 – 7.0 keV band. The shaded area shows the 68% confidence band for parameters. Dashed lines mark the 68% prediction band for T_{500} . Note the absence of errors for the values of T_{500} from the catalogue. Red dots indicate clusters, which parameters are inside the prediction band for derived $T_{500} - E_{\text{av}}$ relation, while blue dots indicate those outside it. The background is not taken into account.

3.3 Average energy

We suggest yet another indicator of a cluster gas temperature - the average energy of counts in the observed X-ray spectra. In this work, if not stated otherwise, we consider this quantity in the same energy band that was used for spectral fitting, i.e. in 0.4 – 7.0 keV. Based on our mock observations we calculate the average energy E_{av} of the observed spectra following Vikhlinin (2006):

$$E_{\text{av}} = \frac{\sum E_i s_i}{\sum s_i}, \quad (3)$$

where s_i is the observed count rate in the channel i and E_i is the nominal energy corresponding to this channel. The count rates s_i depend on the temperature, interstellar absorption, and detector sensitivity as a function of energy. Therefore, the average energies of an observed spectrum calculated for different detectors/telescopes are not necessarily the same. Vikhlinin (2006) used this value as an indicator of temperature only in line-dominated spectra. Here, we extend the applicability of this quantity to realistic X-ray spectra.

In Figure 4, we compare the temperature T_{500} and the average energy E_{av} (in the 0.4 – 7.0 keV band) for each cluster in the sample. We see a strong correlation between the cluster temperature and the average energy of its spectrum what can be easily explained. For clusters with higher temperatures, the exponential cutoff is moving towards high energies; this gives increase in count rate at hard part of X-ray spectrum, thus shifting average energy toward higher values.

The temperature as a function of the average energy can be well described by a power law. The values of parameters were obtained using the orthogonal distance regression (ODR); if not stated otherwise, hereinafter the same procedure is used for power-law fitting. The best-fit function is also presented in Fig. 4 together with pre-

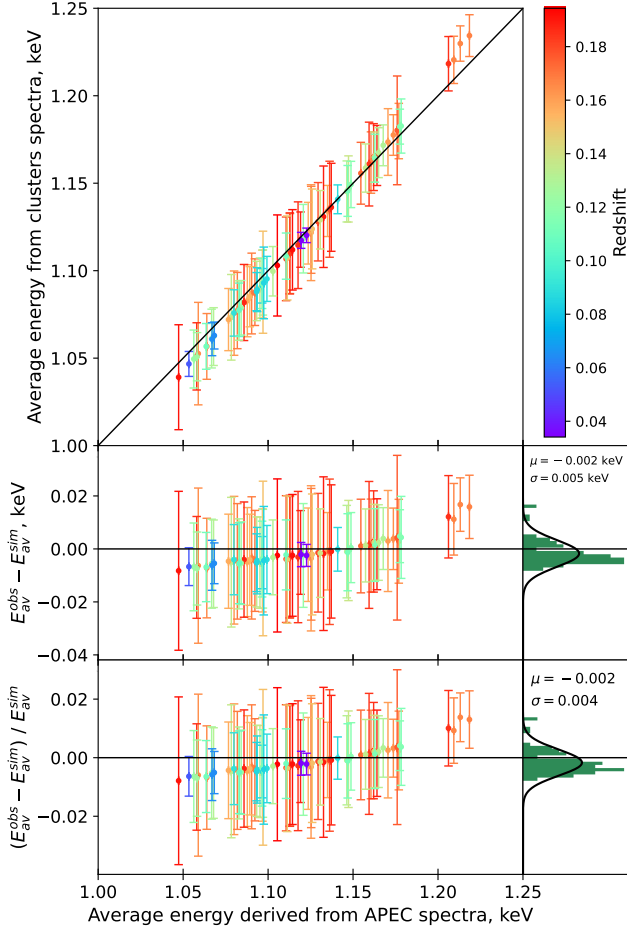


Figure 5. Comparison of average energies: E_{av}^{sim} from simulated single-temperature APEC models with a temperature equal to T_{spec} vs E_{av}^{obs} from spectral fitting for 84 clusters from *Magneticum* simulations. The upper panel compares average energies directly, whereas the central panel compares absolute difference and the lower panel compares relative difference between them. The histograms on the right indicate mean values μ and scatter σ for this comparisons. Redshifts are indicated by colorbar.

diction bands for values of T_{500} . As a result, the value of cluster temperature T_{500} can be written as a function

$$T_{500} = (1.35 \pm 0.04) \text{ keV} \left(\frac{E_{av}}{1 \text{ keV}} \right)^{6.8 \pm 0.3} \quad (4)$$

with a scatter of $\sim 10\%$.

To further illustrate the credibility of using the average energy as a temperature indicator, we simulate single-temperature spectra of each cluster using the APEC model with the following parameters: temperature equal to T_{spec} , abundance of heavy elements $Z = 0.3$ of the Solar value (the abundance tables from [Anders & Grevesse \(1989\)](#) were used), redshift $z = 0$. These spectra were then convolved with *eROSITA* response matrices, and the average energy of the resulting spectrum in the $0.4 - 7.0$ keV band was calculated. In Figure 5, these results are compared for each cluster with values of average energy computed from the cluster spectra extracted from the simulated photon lists. Both values are in a good agreement, which indicates that the single-temperature model offers a very good approximation for the integral cluster spectra.

3.4 Towards realistic spectra

To simulate realistic observations of galaxy clusters with *SRG/eROSITA* we add the astrophysical and particle X-ray background to previously obtained cluster spectra. For both components we use empirical models that describe in-orbit background measurements ([Predehl et al. 2021](#)). The details of simulating background are available in Appendix C. To accurately estimate the contribution of different components to the total observed spectra, we assume that the count rates from both astrophysical and particle background are known with high certainty. For this reason we simulate mock background observations with sufficiently long exposure of 10^4 ks (for one telescope module), which then can be properly added to each cluster (i.e. considering its angular size).

For each cluster the total spectra (cluster + background) is simulated and fitted the same way as described in Section 3.2, and its average energy E_{av}^{tot} (again, in $0.4 - 7.0$ keV band) is calculated. After averaging values of spectral temperatures with background added (we denote this value as T_{spec}^{BKG}) the results are compared with previously obtained values of T_{spec} without background. Temperature comparison is shown in Figure 6. The differences between values of spectral temperature with and without background are very small (this is a consequence of our confidence in the accuracy of the background model), but, however, uncertainties are noticeably larger than for the case without background.

Given the expected count rates from both astrophysical and particle background, we can estimate their fractions in total count rate, which are denoted as n_{ph} and n_{pbkg} respectively, as well as their average energies E_{av}^{ph} and E_{av}^{pbkg} . In this case the expression for average energy of cluster spectra is

$$E_{av}^* = \frac{E_{av}^{tot} - E_{av}^{ph} \cdot n_{ph} - E_{av}^{pbkg} \cdot n_{pbkg}}{1 - n_{ph} - n_{pbkg}} \quad (5)$$

The comparison of T_{500} from the catalogue with average energy E_{av}^* of a cluster in the presence of background and derivation of expression for it is performed similar to the Section 3.3 and is shown in Figure 7. As earlier, the dependence of temperature T_{500} as a function of average energy is well described by power-law

$$T_{500}^{BKG} = (1.29 \pm 0.04) \text{ keV} \left(\frac{E_{av}^*}{1 \text{ keV}} \right)^{7.1 \pm 0.2} \quad (6)$$

with slightly larger scatter than in the case of no background (but still of $\sim 10\%$ order). The best-fit function is also presented in the Fig. 7 together with the confidence and prediction bands. This function is in a good agreement with Equation 4, even with visibly larger errors on E_{av} for the fixed value of temperature. Thus, given proper accounting for the background, the average energy shows robustness as an indicator of a temperature.

4 CLUSTER MASS ESTIMATIONS

To frame the cosmological implications of our work, we compare the scatter of different proxies for mass with each other. At first, we recall the calculation of the X-ray luminosity L_{spec} in the $0.5 - 2.0$ keV band which was performed simultaneous to spectral fitting (that was described in Section 3.2). In Figure 8 (upper panel) we show the $M_{500} - L_{spec}$ relation for our sample of clusters. This could be well described by expression

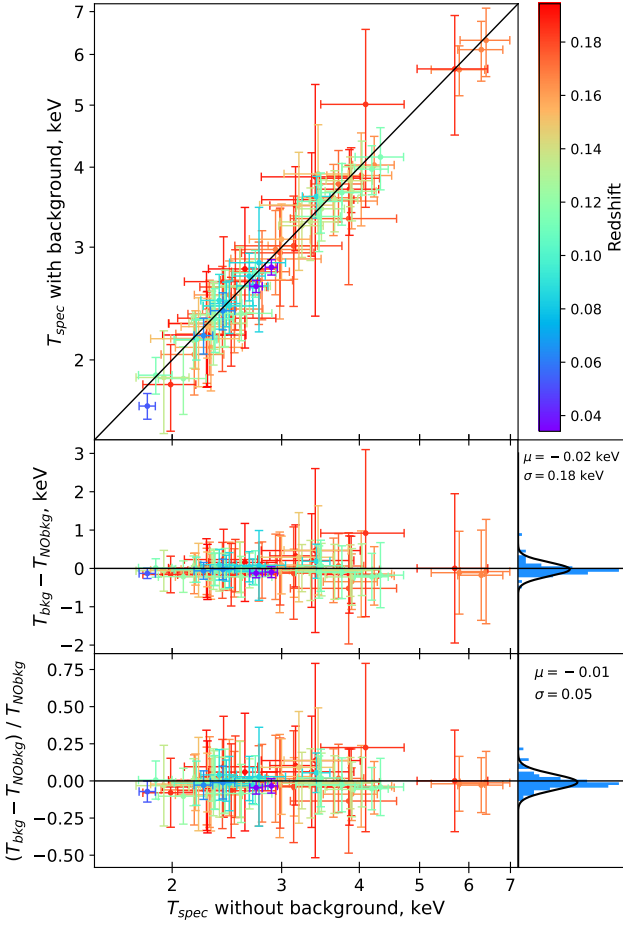


Figure 6. Comparison of temperatures: T_{spec} (without background) vs. $T_{\text{spec}}^{\text{BKG}}$ (with background). The upper panel compares temperatures directly, whereas central panel compares absolute difference and lower panel compares relative difference between them. The histograms on the right indicate mean values μ and scatter σ for these comparisons. Redshifts are indicated by colorbar. Note the log-scale for horizontal axis.

$$M_{500} = (3.66 \pm 0.15) \cdot 10^{14} M_{\odot} h^{-1} \left(\frac{L_{\text{spec}}}{10^{44} \text{ ergs/s}} \right)^{0.74 \pm 0.04} \quad (7)$$

with the scatter of $\sim 21\%$ for a fixed value of luminosity. The scatter of this expression, if it is reversed, translates into $\sim 30\%$ spread of luminosity for a fixed value of mass, which is sufficiently large, but expected value. This dependence shows less scatter than the one implied by Equation 2 and has somewhat smaller slope.

Next, we demonstrate the $M_{500} - T_{\text{spec}}$ relation, which is shown in Figure 8 (central panel) and given by expression

$$M_{500} = (0.35 \pm 0.03) \cdot 10^{14} M_{\odot} h^{-1} \left(\frac{T_{\text{spec}}}{1 \text{ keV}} \right)^{1.47 \pm 0.08} \quad (8)$$

with $\sim 17\%$ scatter. Being inverted, this expression agrees well with Eq. 1, which was previously shown in Figure 2 for $M_{500} - T_{500}$ relation.

Finally, we present the $M_{500} - E_{\text{av}}$ relation. It is also shown in Figure 8 (bottom panel) and described by the expression

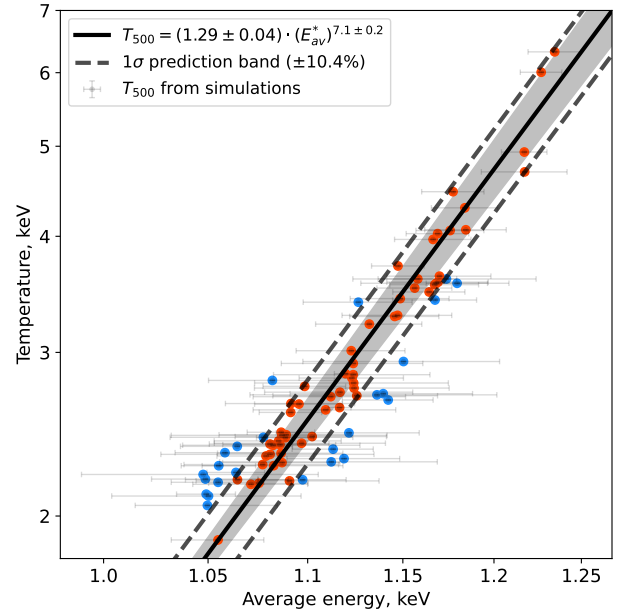


Figure 7. Temperature T_{500} as function of average energy E_{av}^* in the 0.4 – 7.0 keV band. Shaded area is 68% confidence bands for the parameters. Dashed lines show 68% prediction bands for T_{500} . Red dots indicate clusters, which parameters are inside the prediction band for the derived $T_{500} - E_{\text{av}}^*$ relation, while blue dots indicate those outside it. The astrophysical and instrument backgrounds are taken into account in this case.

$$M_{500} = (0.54 \pm 0.03) \cdot 10^{14} M_{\odot} h^{-1} \left(\frac{E_{\text{av}}}{1 \text{ keV}} \right)^{9.7 \pm 0.4} \quad (9)$$

with the scatter of $\sim 19\%$. As for $M_{500} - T_{\text{spec}}$ and $M_{500} - L_{\text{spec}}$ relations, there is hardly any difference between the use of $M_{500} - E_{\text{av}}$ relation obtained from spectra with or without background. Having similar scatter, $M_{500} - E_{\text{av}}$ relation is much easier to obtain because it does not require spectral fitting.

It is a question of interest whether the obtained relations remain the same in case of low count statistics. We have performed the same procedure as before, but the exposure time was reduced to 1 ks of observations for each cluster. As the statistic deteriorate, the measurement scatter of $L_{\text{spec}}, T_{\text{spec}}$ and E_{av} for a fixed mass value grows, but, surprisingly, the scaling relations and their intrinsic scatter keeps almost the same.

Another problem which needs further investigation is selection effects. It can be clearly seen that in each panel of Figure 8 the cluster sample can be divided into two sub-samples. The low-mass group ($M_{500} \approx (1 - 1.5) \cdot 10^{14} M_{\odot} h^{-1}$) tends to shift the overall dependence to higher values of observable quantities for fixed mass, whereas high mass group ($M_{500} > 1.5 \cdot 10^{14} M_{\odot} h^{-1}$) obeys the general slope quite well.

5 CONCLUSIONS

Using a sample of 84 massive galaxy clusters from the *Magneticum* cosmological hydrodynamical simulations, we analysed spectra of their predicted X-ray emission integrated over R_{500} radii and mocked into observational data corresponding to the response functions and exposure time of the *SRG/eROSITA* all-sky survey (including astrophysical and instrumental backgrounds). A simple image-based

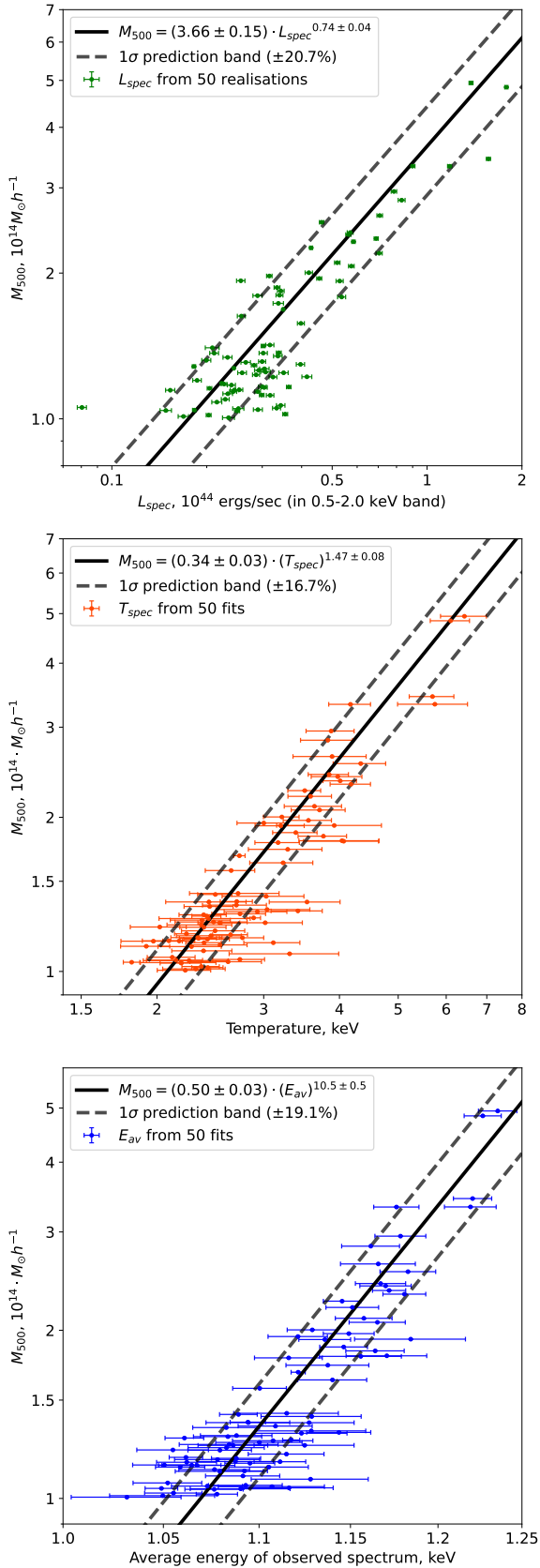


Figure 8. From top to bottom: M_{500} as a function of luminosity L_{spec} (in 0.5 – 2.0 keV band), spectral temperature T_{spec} and average energy E_{av} (in 0.4 – 7.0 keV band). Dashed lines show 68% prediction band.

filtering of the registered counts allows us to obtain almost uncontaminated ICM spectrum (at the affordable cost of losing $\lesssim 25\%$ of the counts), which is shown to be quite well described by single-temperature thermal emission model.

Average energy E_{av} of the detected X-ray spectrum of a cluster in the 0.4–7.0 keV band turns out to be a stable proxy for the ICM mass-weighted temperature T_{500} , being model-independent and insensitive to the properly accounted background contribution.

Relations between the cluster mass M_{500} , its luminosity L_{spec} (in 0.5 – 2.0 keV band), spectral temperature T_{spec} and average energy E_{av} (in 0.4 – 7.0 keV band) have less than 20% statistical scatter, allowing one to use E_{av} as a reliable simple (not requiring spectral fitting) observational proxy for them. Although the exact form of the derived relations obviously depends on the parameters of the X-ray telescope, they can be readily calibrated using the same procedure and taking advantage of the clusters’ spectral database, which is made publicly available with the current study.

ACKNOWLEDGEMENTS

We are thankful to Eugene Churazov for valuable discussions and suggestions.

IK and KD acknowledge support by the COMPLEX project from the European Research Council (ERC) under the European Union’s Horizon 2020 research and innovation program grant agreement ERC-2019-AdG 882679.

DATA AVAILABILITY

The catalogue of *Magneticum* clusters and the corresponding photon lists are publicly available online. The extracted (unfiltered and filtered for bright substructures) cluster images and Radially-Resolved Clusters Spectral Database can be accessed via https://github.com/pi4imu/RRCs_DB.

REFERENCES

- Anders E., Grevesse N., 1989, *Geochimica Cosmochimica Acta*, **53**, 197
- Angelini M., Ettori S., Dolag K., Vazza F., Ragagnin A., 2022, *A&A*, **663**, L6
- Arnaud K. A., 1996, in Jacoby G. H., Barnes J., eds, *Astronomical Society of the Pacific Conference Series Vol. 101, Astronomical Data Analysis Software and Systems V*. p. 17
- Arnaud M., Evrard A. E., 1999, *MNRAS*, **305**, 631
- Beck A. M., et al., 2016, *MNRAS*, **455**, 2110
- Biffi V., Dolag K., Böhringer H., Lemson G., 2012, *MNRAS*, **420**, 3545
- Biffi V., Dolag K., Böhringer H., 2013, *MNRAS*, **428**, 1395
- Biffi V., et al., 2017, *MNRAS*, **468**, 531
- Biffi V., Dolag K., Merloni A., 2018, *MNRAS*, **481**, 2213
- Biffi V., Dolag K., Reiprich T. H., Veronica A., Ramos-Ceja M. E., Bulbul E., Ota N., Ghirardini V., 2022, *A&A*, **661**, A17
- Böhringer H., Werner N., 2010, *A&ARv*, **18**, 127
- Bulbul E., et al., 2019, *ApJ*, **871**, 50
- Churazov E., Vikhlinin A., Sunyaev R., 2015, *MNRAS*, **450**, 1984
- Dolag K., Borgani S., Murante G., Springel V., 2009, *MNRAS*, **399**, 497
- Dolag K., Komatsu E., Sunyaev R., 2016, *MNRAS*, **463**, 1797
- Eckert D., Finoguenov A., Ghirardini V., Grandis S., Kaefer F., Sanders J., Ramos-Ceja M., 2020, *The Open Journal of Astrophysics*, **3**, 12
- Foster A. R., Ji L., Smith R. K., Brickhouse N. S., 2012, *ApJ*, **756**, 128
- Groth F., Steinwandel U. P., Valentini M., Dolag K., 2023, *MNRAS*, **526**, 616
- Hickox R. C., Markevitch M., 2006, *ApJ*, **645**, 95
- Hickox R. C., Markevitch M., 2007a, *ApJ*, **661**, L117

- Hickox R. C., Markevitch M., 2007b, *ApJ*, **671**, 1523
- Hirschmann M., Dolag K., Saro A., Bachmann L., Borgani S., Burkert A., 2014, *MNRAS*, **442**, 2304
- Hoekstra H., 2003, *MNRAS*, **339**, 1155
- Kaiser N., 1986, *MNRAS*, **222**, 323
- Komatsu E., et al., 2011, *ApJS*, **192**, 18
- Kravtsov A. V., Borgani S., 2012, *Annual Review of Astronomy and Astrophysics*, **50**, 353
- Kravtsov A. V., Vikhlinin A., Nagai D., 2006, *ApJ*, **650**, 128
- Lyskova N., Churazov E., Khabibullin I. I., Burenin R., Starobinsky A. A., Sunyaev R., 2023, *MNRAS*, **525**, 898
- Marini I., et al., 2024, *arXiv e-prints*, p. arXiv:2404.12719
- Markevitch M., 1998, *ApJ*, **504**, 27
- Markevitch M., et al., 2003, *ApJ*, **583**, 70
- Mathiesen B. F., Evrard A. E., 2001, *ApJ*, **546**, 100
- Mazzotta P., Rasia E., Moscardini L., Tormen G., 2004, *MNRAS*, **354**, 10
- Meneghetti M., Rasia E., Merten J., Bellagamba F., Ettori S., Mazzotta P., Dolag K., Marri S., 2010, *A&A*, **514**, A93
- Merloni A., et al., 2024, *A&A*, **682**, A34
- Ponti G., et al., 2023, *A&A*, **674**, A195
- Pratt G. W., Croston J. H., Arnaud M., Böhringer H., 2009, *A&A*, **498**, 361
- Predehl P., et al., 2021, *A&A*, **647**, A1
- Sarazin C. L., 1986, *Reviews of Modern Physics*, **58**, 1
- Scheck D., Sanders J. S., Biffi V., Dolag K., Bulbul E., Liu A., 2023, *A&A*, **670**, A33
- Schellenberger G., Reiprich T. H., Lovisari L., Nevalainen J., David L., 2015, *A&A*, **575**, A30
- Seppi R., et al., 2023, *A&A*, **671**, A57
- Springel V., 2005, *MNRAS*, **364**, 1105
- Springel V., White S. D. M., Tormen G., Kauffmann G., 2001, *MNRAS*, **328**, 726
- Sunyaev R. A., Zeldovich Y. B., 1972, *Comments on Astrophysics and Space Physics*, **4**, 173
- Sunyaev R., et al., 2021, *A&A*, **656**, A132
- Vikhlinin A., 2006, *ApJ*, **640**, 710
- Vikhlinin A., et al., 2003, *ApJ*, **590**, 15
- Vikhlinin A., Kravtsov A., Forman W., Jones C., Markevitch M., Murray S. S., Van Speybroeck L., 2006, *ApJ*, **640**, 691
- Vikhlinin A., et al., 2009, *ApJ*, **692**, 1033
- Vladutescu-Zopp S., Biffi V., Dolag K., 2023, *A&A*, **669**, A34
- Zhuravleva I., Churazov E., Kravtsov A., Lau E. T., Nagai D., Sunyaev R., 2013, *MNRAS*, **428**, 3274
- ZuHone J., et al., 2023, *A&A*, **675**, A150

APPENDIX A: DATABASE OF X-RAY IMAGES AND RADIALLY-RESOLVED SPECTRA OF CLUSTERS

The examples of original and filtered images of three different studied galaxy clusters at $z = \{0.035, 0.089, 0.157\}$ are shown in Figure A1. The filtering procedure is described in Section 3.1. In each image there is a circle with the radius equal to R_{500} for this cluster with its center located at centroid of the image; there is also point indicating position of gravitational potential minimum from *Magneticum* catalogue.

We present the database which contains all 84 clusters' images (both unfiltered and filtered) and their spectra. Description of image development and filtering procedure is given in Section 3.1. After filtering, for each cluster the extracted photons are binned by energies over a range from 0.1 to 12.0 keV in 4096 logarithmic steps, which results in flux density spectra. All model spectra are stored in single FITS-file, which can be passed as an input to XSPEC software (Arnaud 1996). For spectral models in this database, the overall normalization has been set as if each cluster were 100 Mpc distant.

The examples of X-ray cluster spectra along with the best-fit model

and added background are shown in Figure A2. The fitting procedure is described in Section 3.2.

APPENDIX B: ESTIMATION OF THE STATISTICAL UNCERTAINTIES

To reduce statistical uncertainties in values of temperature, luminosity and average energy, simulated spectrum fitting procedures is performed 50 times for each cluster, and mean value of spectral temperature distribution were considered as true values. Concurrently, we calculated second, third and fourth moments of these distributions (variance, skewness and kurtosis, respectively). In Figure B1 we present values of these moments as functions of increasing number of fitting realisations (up to 100) for 7 distinctive clusters. While the mean value is reached rather quickly as averaging proceeds, other moments demonstrate non-normal distribution behaviour even in case of sufficiently enough realisations. The same procedure was simultaneously performed for luminosity and average energy, and they demonstrate similar behaviour.

APPENDIX C: MODELS FOR BACKGROUND

To simulate astrophysical and particle X-ray background we have used empirical models that describe in-orbit background measurements performed by *SRG/eROSITA* (Predehl et al. 2021).

In particular, the model for particle background we implement, is derived from the released filter wheel closed data measurements (Predehl et al. 2021), which have been shown to provide an excellent agreement with the survey-averaged instrumental background level (e.g. Lyskova et al. 2023).

The model for the astrophysical background consists of four components, including Local Bubble emission, Galactic hot halo and "corona" X-ray Galactic emission, and unresolved point X-ray sources, i.e. Cosmic X-ray background (CXB, we assume that only half of it is resolved), as motivated by previous observations by *Chandra* (Hickox & Markevitch 2006, 2007a,b; Markevitch et al. 2003) and *eROSITA* (Ponti et al. 2023). The first three components can be well described by a thin-thermal plasma and modeled by APEC model with temperatures and normalizations equal to (0.099 keV, 0.00174), (0.225 keV, 0.0007475), (0.7 keV, 0.0000897), redshift equal to 0 and metallicity equal to 1 Solar, Galactic absorbing column equal to $0.018 \cdot 10^{22} \text{cm}^{-2}$. The latter component is described by power law with photon index equal to 1.47 and normalization equal to 0.0001052. We have implemented the photon background as the model for XSPEC in the following form:

$$\text{const}(1) * (\text{apec}(2) + \text{wabs}(3) * (\text{apec}(4) + \text{apec}(5) + \text{const}(6) * \text{powerlaw}(7)))$$

This model is normalized for 1 min². To simulate the background flux corresponding to the aperture of a particular cluster, the flux from this model must be multiplied by projected area of its R_{500} radius in square minutes. During spectral fitting procedure, all components are frozen, but overall normalisation is considered as a free parameter.

This paper has been typeset from a $\text{\TeX}/\text{\LaTeX}$ file prepared by the author.

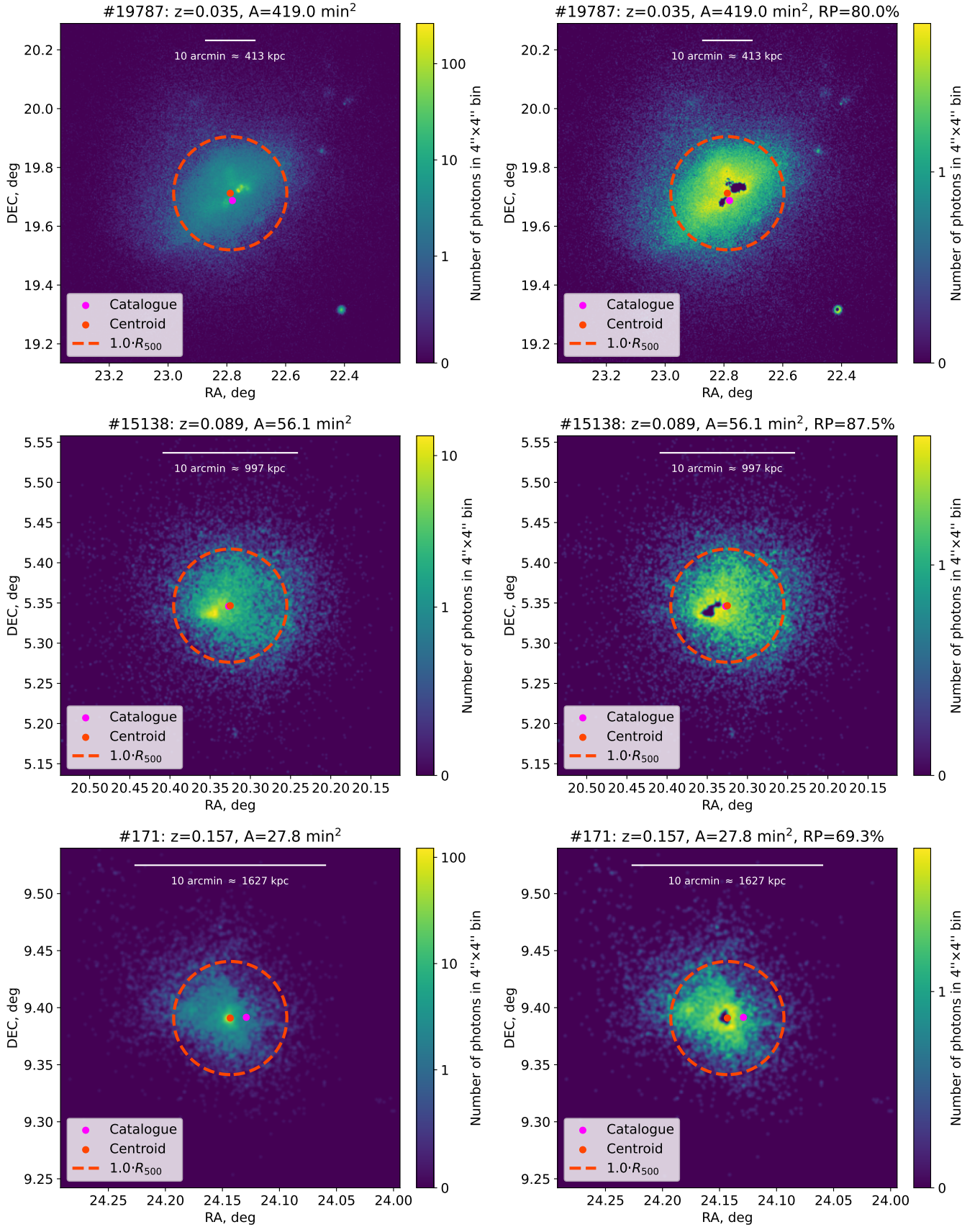


Figure A1. Examples of clusters images at $z = 0.035, 0.089$ and 0.157 (from top to bottom). The left panel in each row shows image obtained with all the photons from the corresponding photon list, whereas the right panels show filtered images. A is the area of circle with radius equal to R_{500} and RP is the fraction of remaining photons after filtering.

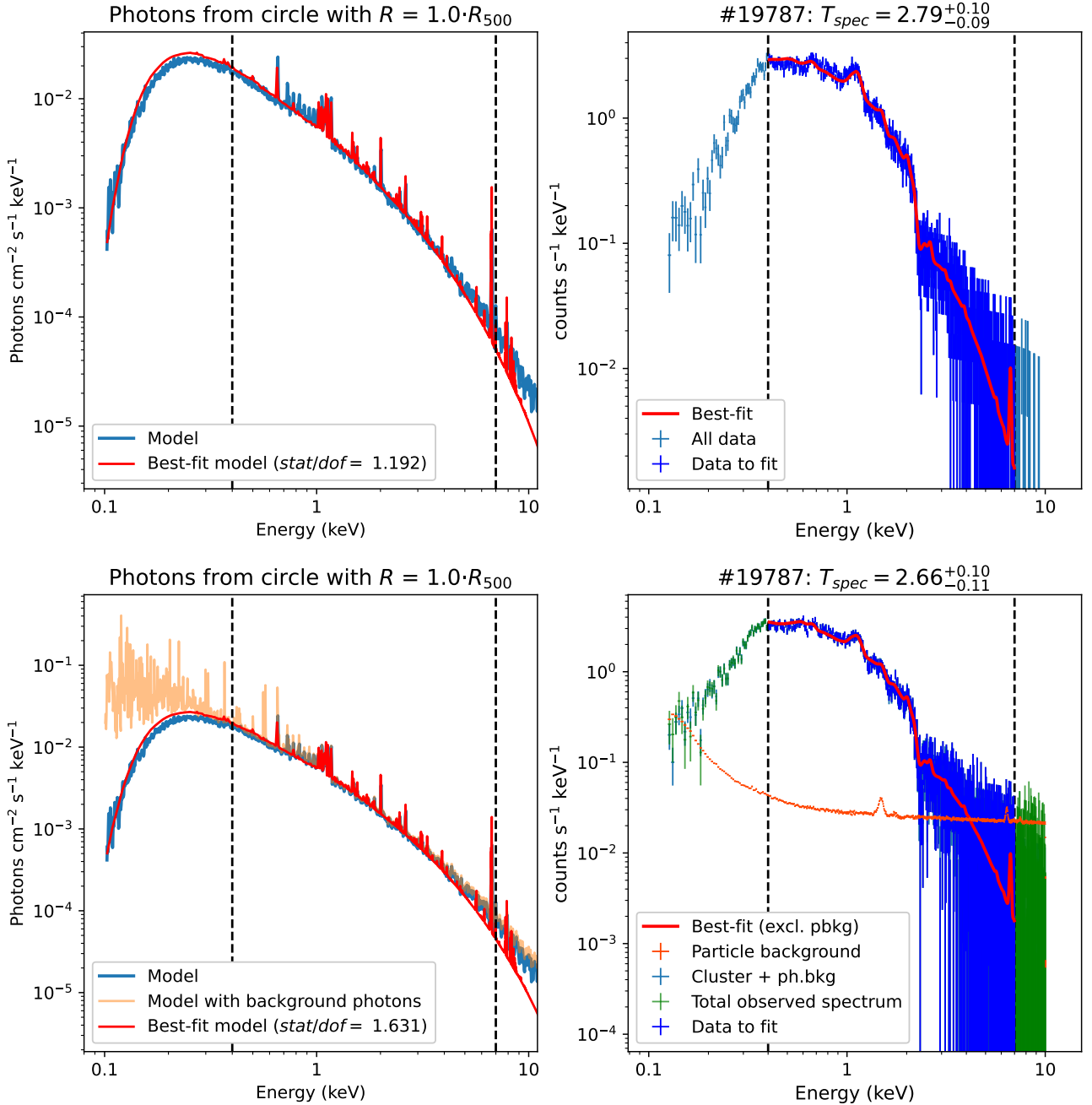


Figure A2. Examples of spectral analysis of cluster #19787. Top and bottom rows show cases without and with background, respectively. In each row the left panel shows model spectra (X-ray flux density) and the best-fit model. The latter is obtained by fitting the mock observed spectrum, which is shown in the right panel, in 0.4 – 7.0 keV energy band. The bottom row also shows the contributions of astrophysical background (on the left panel) and particle background (on the right panel).

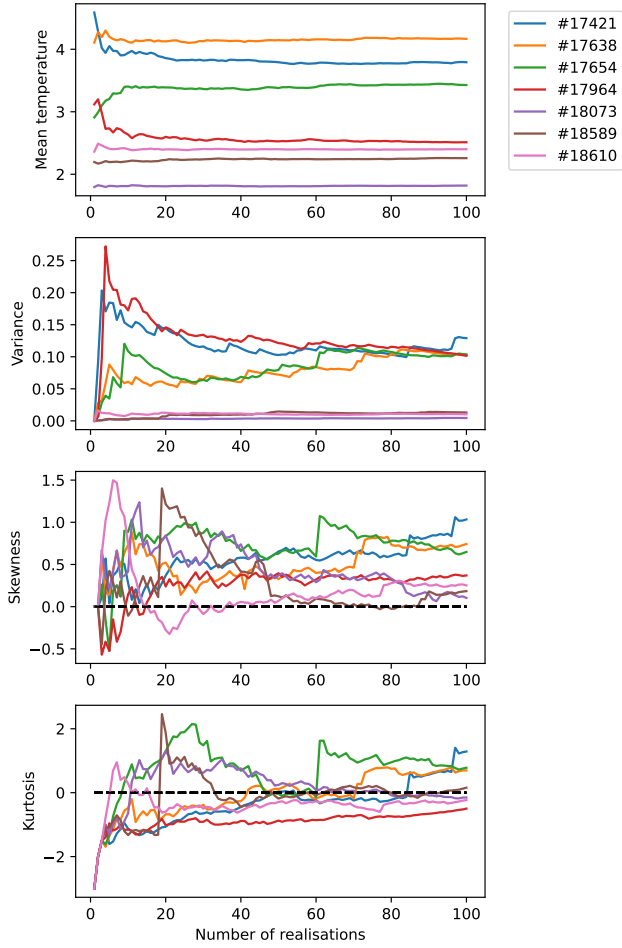


Figure B1. Moments of temperature distribution from first (*upper panel*) to fourth (*bottom panel*) as a functions of increasing number of fitting realisations. Different colors indicate 7 clusters and correspond to their numbers in *Magneticum* catalogue.